Noname manuscript No.
(will be inserted by the editor)

Single-Phase Mixing Through a Narrow Gap

Simo A. Mäkiharju · Seongjin Yoon · Alexander G. Mychkovsky · John R. Buchanan, Jr · Steven L. Ceccio

Received: date / Accepted: date

Abstract Mixing through narrow gaps connecting adjacent flow paths is an important mass and heat transfer process for many thermo−hydraulic applications. Such flows are considered balanced when the inlet flow speeds of adjacent subchannels are matched. In the present work, experimental observations are presented for balanced and unbalanced flows including the mixing coefficients and flow visualization within the gap. The large coherent structures are identified, with frequency in general agreement with those reported by previous investigators. To utilize Proper Orthogonal Decomposition (POD) for the discrete data yielded by PIV, we employ method of Singular Value Decomposition (SVD). The bulk of the mixing is attributed to the dominant modes and demonstrate that mixing rates estimated from velocity measurements are in fair agreement with mixing coefficients based on tracer concentration measurements.

Keywords Mixing · Coherent structures · Proper Orthogonal Decomposition

Simo A. Mäkiharju
6119 Etcheverry Hall
University of California, Berkeley, CA 94720, USA
E-mail: makiharju@berkeley.edu

Seongjin Yoon
University of Michigan, Ann Arbor, MI 48109, USA

Alexander G. Mychkovsky
Naval Nuclear Laboratory, West Mifflin, PA 15122, USA

John R. Buchanan, Jr.
Naval Nuclear Laboratory, West Mifflin, PA 15122, USA

Steven L. Ceccio
1221 Beal Avenue
University of Michigan, Ann Arbor, MI 48109, USA

1 Introduction

Mixing through narrow gaps connecting adjacent flow paths may result from pressure gradients across the gap (due to unbalanced inflow or a back-pressure differential), small scale turbulence in the gap, or the development of large-scale, periodic flow structures resulting from the shear between flow in gap and subchannel. The presence of these large-scale, coherent flow structures can drastically influence the rate of mixing. (We define as balanced conditions having equal flow speeds, and Reynolds numbers, at both sub-channel inlets. Whereas for unbalanced flows, the inlet Reynolds numbers are not matched.)

Several researchers have experimentally studied the flows in parallel channels connected by narrow gaps [1, 2, 3, 4, 5, 6, 7, 8]. In particular, Meyer [8] provides a review of inter-channel mixing, and discusses the underlying flow processes, including the large-scale coherent structures. Inter-channel mixing has also been numerically investigated by several researchers, including Chang and Tavoularis [9] [10], Home *et al.* [11], Derksen [12], and Home and Lightstone [13]. Merzari *et al.* [14] also used Proper Orthogonal Decomposition (POD) on numerical and experimental data to explore the underlying dynamics of the flow oscillations observed in the inter-channel flow.

As more advanced numerical models for thermo-hydraulic applications are developed, there is an increasing need for validation data. However, few studies have produced experimental data sets of mixing through narrow gaps that are readily suitable for the validation of high-fidelity simulations. In particular, these flows are sensitive to small changes in boundary conditions (for example, Ko *et al.* [15] demonstrates such sensitivity of a similar flow).

This paper presents an extension of the work reported in Mäkiharju *et al.* [16] and Yoon [17], in which the flow in a canonical geometry was investigated. The inlet flow conditions were extensively surveyed *via* Laser Doppler Velocimetry (LDV) and the bulk mass transfer through the narrow gap determined based on fluid mass flow rate and fluorescein tracer dye concentration measurements at the channel inlets and outlets. These measurements were conducted for varying gap dimension and flow rates. Particle Image Velocimetry (PIV) was employed to visualize the flow within the gap at select conditions to examine the dynamics of the mixing phenomena. Singular Value Decomposition (SVD) was utilized to analyze the PIV data by decomposing the flow field and to identify the most energetic coherent structures in the gap. Subsequently, the strongest SVD modes were used to estimate the mixing rate, which had satisfactory agreement with mixing determined more directly from measurements of dye concentration. In addition to providing another way to estimate the mixing rate, this approach allows us to determine which structures account for the majority of the mixing.

The experimental setup and the inflow conditions are described in §2. The time averaged results of integral mixing of both balanced and unbalanced inlet mass flow rates are presented in §3. The flow structures within the gap between the channels using SVD are examined in §4, and data used to estimate the mixing coefficient in §5. Details of the observed coherent structures based on analysis of the PIV data is provided in §4, and the estimation of the mixing coefficients based on the PIV in §5. Finally, §6 summarizes the findings.

2 Experimental Setup

The flow loop was developed to examine the inter-channel mixing between two, parallel channels with square cross sections connected by a rectangular gap, as shown in Fig. 1. Both channel A and B have cross-section dimensions of 127 mm × 127 mm. The hydraulic diameter D_h, defined as $D_h = 4A_w/P_w$ where A_w is the cross-sectional area and P_w is the wetted perimeter of the channel, is 127 mm for each channel. The gap width W_g and length L_g are fixed at 228.6 mm and 1219.2 mm, respectively. The gap height H_g can be varied from 0 to 50 mm.

Figure 2 shows the flow loop's piping and instrumentation diagram.

The flow into each channel was conditioned with a series of pressure drop plates, a flow straightener, mesh and a 6-to-1 asymmetric contraction. This led to a low turbulence inflow into the channels without significant swirl. The contraction was followed by boundary layer

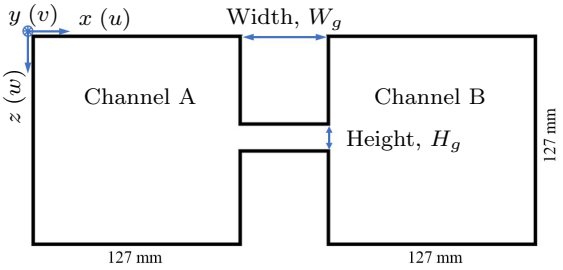

Fig. 1 Cross-sectional geometry of the test section and the coordinate system used for the boundary layer description. Axes convention follows the right hand rule, with the origin $y = 0$ defined at the beginning of the gap, and origin at the center of the gap (axis offset in figure for clarity).

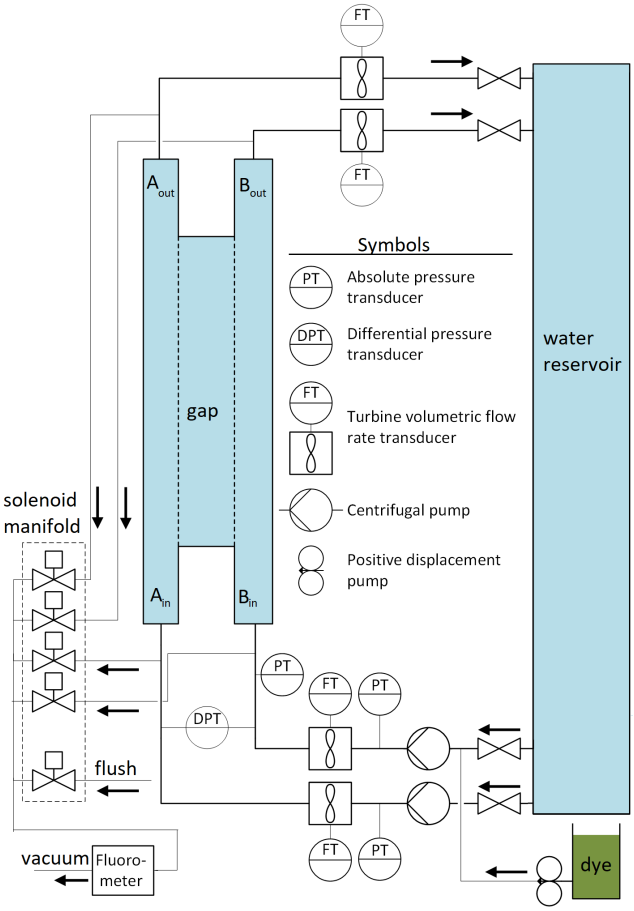

Fig. 2 Piping and instrument diagram of the flow loop.

trips to hasten the transition to a turbulent boundary layer on the walls of the channels. Fig. 3 shows the detailed drawing of the test section, contraction, flow conditioner, and trip plate; Fig. 4 identified the fields-of-view (FOVs) used for the PIV measurements.

Two independently controlled pumps produced the flow into each channel. Both pumps were controlled by Yaskawa E7 variable frequency drives (E7LVD024CFX) and drew water from a shared 17 m^3 reservoir. The flow was returned to the reservoir after passing through the

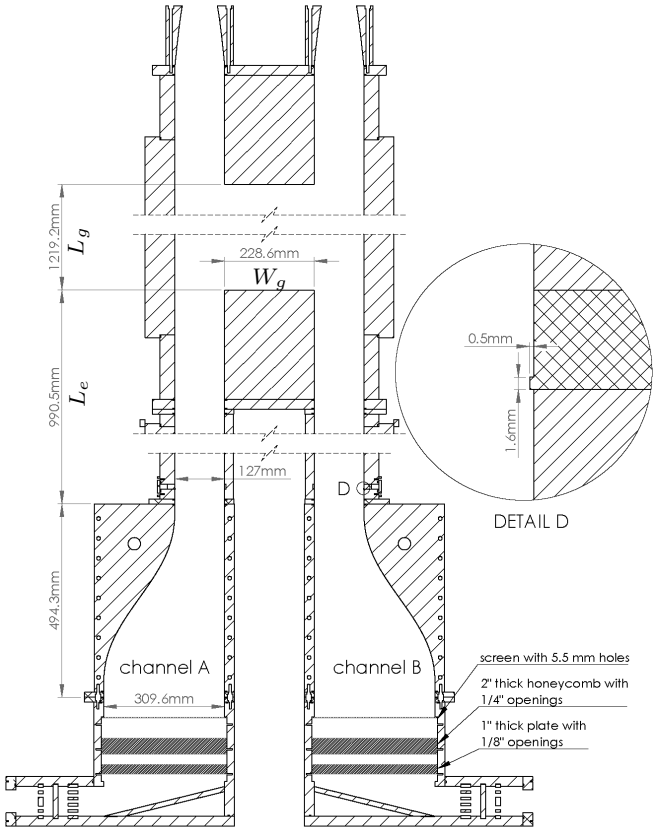

Fig. 3 Geometry of the test section and flow conditioners, with the trip plate shown in detail D. The coordinate system origin ($x = y = 0$) is defined at the center, bottom plane of the gap. (Note that the coordinate system of PIV is different from that of LDV shown in Fig. 5.) All dimensions are in millimeters, and absolute positions accurate within ±2 mm.

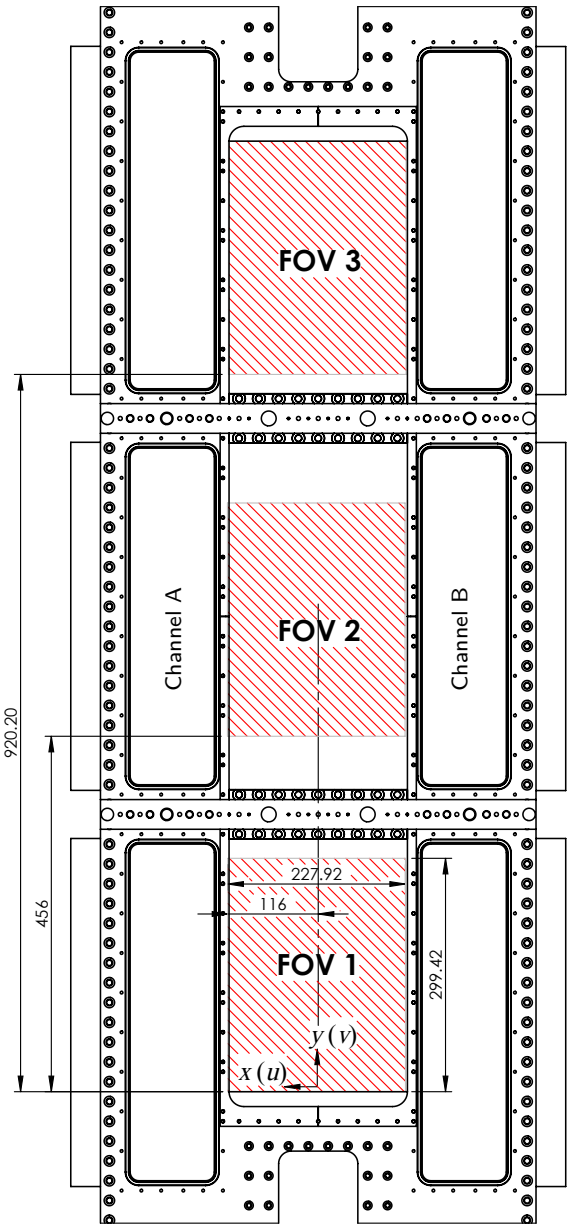

Fig. 4 The three fields of view (FOV) used for the PIV. Note the gaps between the FOVs are areas blocked by structure and are not accessible for PIV.

test section. The volume flow rates at the test section inlets were measured with Omega Engineering SYS/FTB-109/FLSC-18B turbine flow meters with mfg. specified accuracy of ±0.5 % of reading. The volume flow rates at the outlets were measured with two Omega Engineering FTB740 turbine flow meter with FTB700 transmitters with manufacturer specified accuracy of ±1 % FS (±6 gpm).

The water temperature at both inlets and outlets was measured by four 4-wire 100 Ohm platinum Resistance Temperature Detector (RTD) sensor P-M-A-1/4-6-0-P-3 with a specified accuracy $\pm(0.15 + 0.002|T|)$ °C from -100 to 450 °C. The RTD was periodically compared against an ice bath, and found to be accurate within 0.4 °C (consistently giving a high reading), and at room temperature agreed with a Mannix DLAF-8000 to within 0.3 °C.

The pressure immediately downstream of the boundary layer trip in channel B was continuously measured with an absolute pressure transducer Omega Engineering PX219-030A10V (with PS-4E snubber) and a manufacturer specified accuracy of ±0.25 % FS. Static pressures at outlets of both pumps and at the beginning of the flow conditioners (measured solely for system performance monitoring and operator safety) were measured with Omega Engineering PX303-200G5V with a specified accuracy of ±0.25 % BFSL (±0.5 psi). The critical pressure difference between sides A and B, 6.45 D_h (32.25 inches) upstream of the gap was measured with an Omega Engineering PX760-06WCDI with a specified accuracy ±0.17 % FS of nominal range, and also measured using water-air manometers with esti-

mated accuracy of ±0.03 inches (±0.76 mm) H_2O. The lines to both transducers were periodically flushed to remove any gas bubbles.

2.1 Inflow Conditions

The Reynolds number based on the channel's hydraulic diameter in both channel inlets was varied from Re = 4×10^4, 6×10^4, 8×10^4, to 1×10^5. With 20 °C water, this corresponds to average inlet flow speeds into the channels of 0.32, 0.47, 0.63 and 0.79 m/s, respectively. For balanced cases the inflow Re of both sub-channels are equal, and all four Reynolds numbers listed above were studied, with this paper presenting data for lowest and highest Re. For the unbalanced flows, focus was on sub-channel A with inlet $\mathrm{Re}_A = 10^5$ and sub-channel B with Re_B = 4, 6 and 8 x10^4.

The flow conditions in the channels upstream of the gap, but downstream of the boundary layer trip, were surveyed using two dimensional Laser Doppler Velocimetry (LDV) measurements of the axial flow velocity. LDV measurements were conducted when the inter-channel gap was closed. Fig. 5 presents the boundary layer profiles of the inflow. The shape factor H_s is 1.4 for the turbulent flow, and 2.6 for the laminar flow [18], the near wall flow profiles indicate that the boundary later is laminar/transitional at the lowest Reynolds number, and becomes turbulent at the higher values. For the flow conditions investigated the boundary layer shape factor was found to be 1.5 for all cases, except Re = 4×10^4 for which the shape factor was 2.4. (Additional detail including fluctuating quantities are reported in Mäkiharju *et al.* 2015 [16].)

2.2 Measurement of Inter-Channel Mixing

The transport and dilution of tracer dye was used to measure the inter-channel mixing. The bulk mixing coefficients were calculated based on measurements of the concentration of fluorescein sodium salt (F6377, Sigma-Aldrich) at the inlets and outlets of the two channels. The dye was injected immediately upstream of the B-side pump using a Pulsatron ChemTech dual-head Peristaltic Pump (model XP100-LG-LX) that according to specifications provides a flow rate repeatable within ±5 %. The dye concentration of samples drawn from the flow was measured with a Turner Designs Cyclops 7 (C7) fluorometer. Additionally, a secondary custom fluorometer was used to compare against C7 to detect anomalous readings as they occurred (*e.g.* due to bubbles getting lodged in the C7 sample chamber). Based

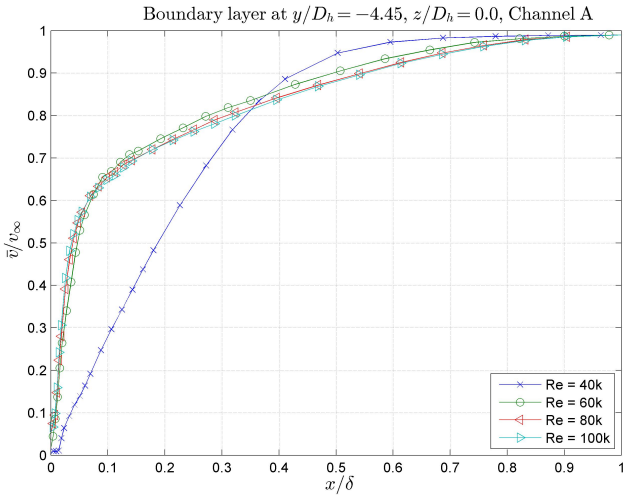

Fig. 5 Boundary layer profiles at $y/D_h = -4.45$ in channel A. The origin $y = 0$ is defined at the beginning of the gap [16] and for convenience x is set to zero on the channel wall.

on calibration with samples of known dye concentration, the uncertainty of the C7 fluorometer was determined to be ±0.5 % of the reading. The injection of dye also permitted qualitative visualization the flow structures in the gap and within the channel, as shown in Fig. 6.

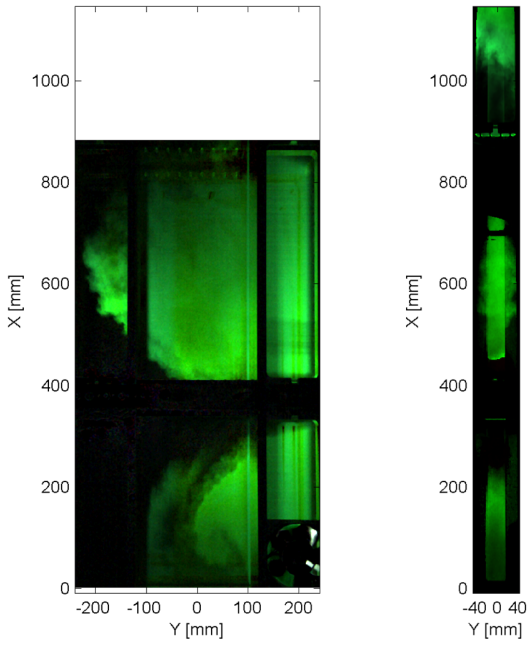

Fig. 6 Large structures made visibly by dye for balanced flow Re=[10 10]×10^4 with 50 mm gap height. Left: looking at the two channels and gap with portions of FOV 1 and 2 visible. Right: looking into the gap from channel A side with portions of the three FOV's visible.

2.3 Flow Field Measurements in the Mixing Gap

Two component planar PIV was used to obtain the velocity field data within the gap between the channels Due to the the long gap length, independent PIV data sets were acquired at the 3 FOV locations show in Fig. 4. For the test section discussed in this paper, PIV was recorded for the three FOVs with 10, 20 and 50 mm gap heights, and for [Re_A Re_B], henceforward referred to for brevity as Re,= [4 4], [10 10], [4 10], [6 10] and [8 10] $\times 10^4$, at 12 Hz, 4,000 image pairs per location and condition with 223 x 298 mm FOV size. Fig. 4 shows the location of the FOVs in the gap window with respect to the origin at the center bottom of the gap. A laser light sheet was located at the center plane of the gap, and the PIV images were recorded with DaVis 7.2.2.470 and processed with DaVis 8.1.4.36762 from LaVision Inc. The seeding particles were nominally 12 micron hollow glass beads. The camera was an ImagerPro with 1600 × 1200 pixel resolution and 12-bit depth, and a Nikon 28mm 1:2.8D AF Nikkor lens. Illumination was provided by a Nd:YAG Dual Cavity pulsed laser - Quantel Evergreen PIV 200, 2 x 200 mJ/pulse at 532 nm, 15 Hz pulse rate connected to a light arm that traversed alongside the camera on Linos rails.

The time-averages were subtracted from the instantaneous vector fields, and a geometric mask applied to remove any test section structure seen in the images. The velocity vector calculations utilized Davis' GPU Multi-pass cross-correlation, with first a 128×128, square, 25% overlap, maximum shift of 30 pixels, down to a fourth pass with 32×32, square, 25% overlap, maximum shift 4 pixels. Median and smoothing filters were applied to the final vector fields.

3 Time-Averaged Inter-Channel Mixing

The average amount of mixing between the two channels for varying flow conditions and gap heights was determined through the measurement of dye transport. The mixing coefficient f_A is defined as the time-averaged fraction of water transferred from channel A to B, and f_B is the time-averaged fraction of water transferred from Channel B to A. These are calculated based on the conservation of water mass and the mass of the tracer dye in a fixed control volume.

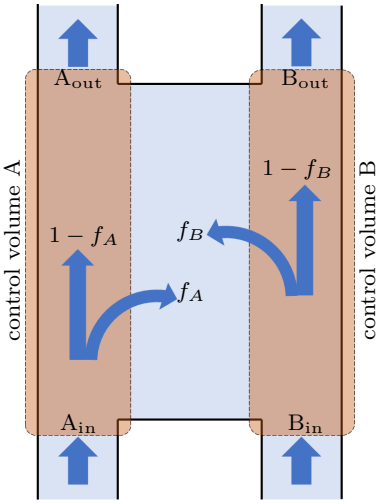

Fig. 7 Schematic drawing of the mixing through the narrow gap with test section, inlets, outlets and control volumes (not drawn to scale).

3.1 Control Volume Analysis to Determine the Inter-Channel Mixing

A control volume encompassing the entire test section, defining a control volume for each channel is shown in Fig. 7.

Based on mass conservation of both water and dye in control volumes A and B, shown in Fig. 7, the following four equations can be written

$$\dot{m}_{AO} = \dot{m}_{AI}(1 - f_A) + \dot{m}_{BI} f_B \quad (1)$$

$$\dot{m}_{BO} = \dot{m}_{AI} f_A + \dot{m}_{BI}(1 - f_B) \quad (2)$$

$$\dot{m}_{AO} C_{AO} = \dot{m}_{AI} C_{AI}(1 - f_A) + \dot{m}_{BI} C_{BI} f_B \quad (3)$$

$$\dot{m}_{BO} C_{BO} = \dot{m}_{AI} C_{AI} f_A + \dot{m}_{BI} C_{BI}(1 - f_B) \quad (4)$$

where $\dot{m}$ is the mass flow rate in kg/s, and C is the tracer concentration in units of kg of tracer per kg of water. Water mass flow rates are calculated based on the volume flow meter readings and density of water at loop temperature. From the sum of Eqn. (1) and (2), and (3) and (4), the mass conservation equations of the water and dye in the global control volume can be written as

$$\dot{m}_{AO} + \dot{m}_{BO} = \dot{m}_{AI} + \dot{m}_{BI}, \quad (5)$$

$$\dot{m}_{AO} C_{AO} + \dot{m}_{BO} C_{BO} = \dot{m}_{AI} C_{AI} + \dot{m}_{BI} C_{BI}. \quad (6)$$

As the system is over-determined with four independent equations for two unknowns, f_A and f_B, four possible sets of solutions can be derived.

$$f_A^{(1)} = 1 - \frac{\dot{m}_{AO}(C_{AO} - C_{BI})}{\dot{m}_{AI}(C_{AI} - C_{BI})}, \quad (7)$$

$$f_B^{(1)} = \frac{\dot{m}_{AO}(C_{AI} - C_{AO})}{\dot{m}_{BI}(C_{AI} - C_{BI})}, \quad (8)$$

$$f_A^{(2)} = \frac{\dot{m}_{BO}(C_{BO} - C_{BI})}{\dot{m}_{AI}(C_{AI} - C_{BI})}, \quad (9)$$

$$f_B^{(2)} = 1 - \frac{\dot{m}_{BO}(C_{AI} - C_{BO})}{\dot{m}_{BI}(C_{AI} - C_{BI})}, \quad (10)$$

$$f_A^{(3)} = \frac{-\dot{m}_{AI}C_{BI} + \dot{m}_{AO}C_{BI} - \dot{m}_{BI}C_{BI} + \dot{m}_{BO}C_{BO}}{\dot{m}_{AI}(C_{AI} - C_{BI})}, \quad (11)$$

$$f_B^{(3)} = \frac{-\dot{m}_{AI}C_{AI} + \dot{m}_{AO}C_{AI} - \dot{m}_{BI}C_{BI} + \dot{m}_{BO}C_{BO}}{\dot{m}_{BI}(C_{AI} - C_{BI})}, \quad (12)$$

$$f_A^{(4)} = \frac{\dot{m}_{AI}C_{AI} - \dot{m}_{AO}C_{AO} + \dot{m}_{BI}C_{BI} - \dot{m}_{BO}C_{BI}}{\dot{m}_{AI}(C_{AI} - C_{BI})}, \quad (13)$$

$$f_B^{(4)} = \frac{\dot{m}_{AI}C_{AI} - \dot{m}_{AO}C_{AO} + \dot{m}_{BI}C_{AI} - \dot{m}_{BO}C_{AI}}{\dot{m}_{BI}(C_{AI} - C_{BI})}. \quad (14)$$

When the measured data are entered into these equations, the resulting mixing coefficients do not match exactly between the four methods of computation due to measurement uncertainties. For simplicity, averaged values of the four sets of $f_A^{(i)}$ and $f_B^{(i)}$ derived in Eqn. (7) to (14) are used as a final coefficient presented for $\overline{f}_A$ and $\overline{f}_B$ in the following sections. The uncertainty of the mixing coefficient f_A, $\delta f_A^{(i)}$, can be estimated based Gauss's Formula (GUM's Linear Approximation) [19]. Assuming all measurements are independent, the uncertainty for $f_A^{(i)}$ can be computed as :

$$\delta {f_A^{(i)}}^2 = \sum_j \left(\frac{\partial f_A^{(i)}}{\partial \dot{m}_j}\right)^2 \delta \dot{m}_j^2 + \sum_j \left(\frac{\partial f_A^{(i)}}{\partial C_j}\right)^2 \delta {C_j}^2. \quad (15)$$

Where $j = AI, AO, BI, BO$.

3.2 The Measured Inter-Channel Mixing Coefficients

The above relationships were used to compute the inter-channel mixing coefficients for the balanced and unbalanced flow conditions and for different gap heights. Fig. 8 presents the coefficient as a function of gap height for the balanced flow with Re = [10, 10]×10^4, and Fig. 9 presents the balanced flow data for Re = [4, 4]×10^4. The coefficients shown by filled symbols are based on SVD data (the sum of the steady and dynamic mixing coefficients, $f^{(s)}$ and $f^{(d)}$ given in tables 1 and 2). and further discussed in §5.

Fig. 10 shows the average mixing coefficients based on tracer dye measurements for the four balanced cases.

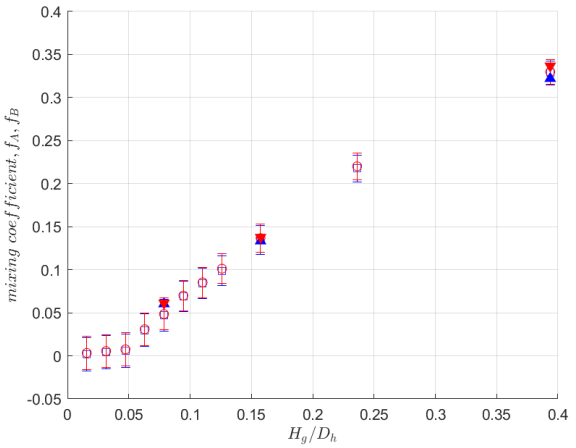

Fig. 8 Comparison of mixing coefficients f_A and f_B of Re = [10, 10]×10^4 based on the dye concentration and the SVD of the PIV data; blue square:f_A based on the dye concentration, red circle:f_B based on the dye concentration, blue triangle: f_A based on the SVD of the PIV data, red downward triangle: f_B based on the SVD of the PIV data.

The mixing shows little dependence on the Reynolds number, with no discernible difference for $H_g/D_h > 0.15$. A linear trend of increasing mixing with increasing gap is maintained until the width of the gap $H_g/D_h > 0.25$. This is presumably due to finite size of channels relative to flow structures, as narrower gap studied in [16] shows a continuing linear trend. When gap width is small producing structures that do not as fully fill the channel by end of test section. For gap widths between $0.05 < H_g/D_h < 0.15$, the mixing coefficients show some Reynolds number dependence. There was little to no mixing within the uncertainty of the measurement for $H_g/D_h < 0.05$, albeit detectable trace amounts of dye was found in Channel A in many cases. For all the balanced cases, the vortical structures within the gap were responsible for the bulk of the mixing, and these structures were suppressed when $H_g/W_g < 0.03$ ($H_g/D_h < 0.05$).

For unbalanced flow, the mixing resulted from both coherent structures and the presence of an average pressure difference across the gap, with the latter effect increasing in importance at smaller gap heights. Figs. 11, 12, and 13 present the mixing coefficient as a function of gap height for the unbalanced flows with Re = [8, 10]×10^4, Re = [6, 10]×10^4, and Re = [4, 10]×10^4. The mixing between channels A and B is no longer symmetric, as expected. If the mixing results from only a one-way mass transfer from channel B to channel A, and results in balanced flow by the end of the gap, the mixing coefficient would be given by:

$$f_A = 0, \text{ and } f_B = \frac{1}{2}\left(1 - \frac{\dot{m}_{AI}}{\dot{m}_{BI}}\right). \quad (16)$$

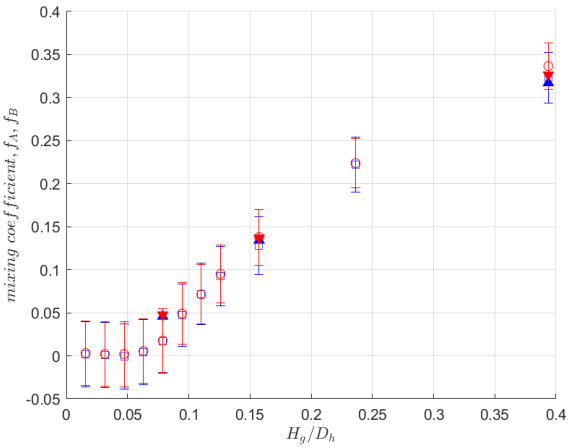

Fig. 9 Comparison of mixing coefficients f_A and f_B of Re = [4, 4]×10^4 based on the dye concentration and the SVD of the PIV data; blue square: f_A based on the dye concentration, red circle: f_B based on the dye concentration, blue triangle: f_A based on the SVD of the PIV data, red downward triangle: f_B based on the SVD of the PIV data.

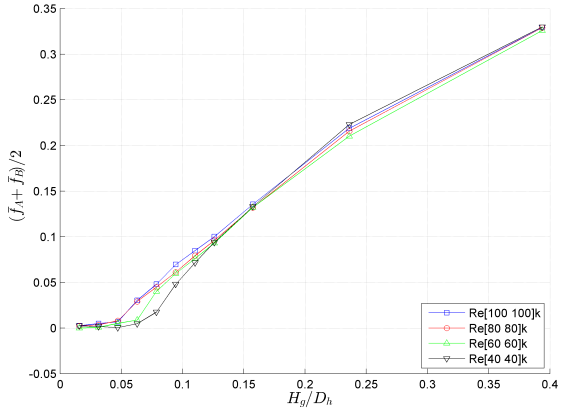

Fig. 10 The average mixing coefficients for all balanced flow cases as a function of gap width. The uncertainty bars are omitted for clarity.

The horizontal line in the mixing coefficient figured represents the value yielded by Eqn. 16, thus showing the asymptotic amount of mixing that would result solely from the pressure difference. This is close to the measured coefficient for the smaller gaps $H_g/D_h <\approx 0.1$ ($H_g/W_g <\approx 0.05$). As the gap size increases and/or the Reynolds numbers increases, the rate of mixing also increases. This is due to the increasing importance of the coherent structures to the overall mixing process.

Also shown in Figs. 8 through 13 are triangular symbols that represent the mixing coefficient estimate based on the SVD of centerline PIV data. The methods and analysis used to derive these companion results is presented below.

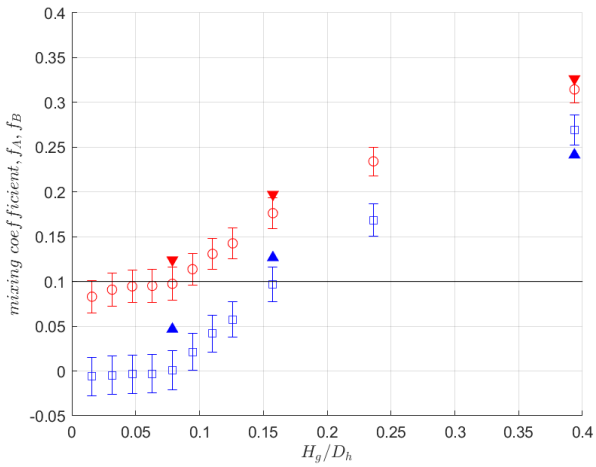

Fig. 11 Comparison of mixing coefficients f_A and f_B of Re = [8, 10]×10^4 based on the dye concentration and the SVD of the PIV data; blue square: f_A based on the dye concentration, red circle: f_B based on the dye concentration, blue triangle: f_A based on the SVD of the PIV data, red downward triangle: f_B based on the SVD of the PIV data.

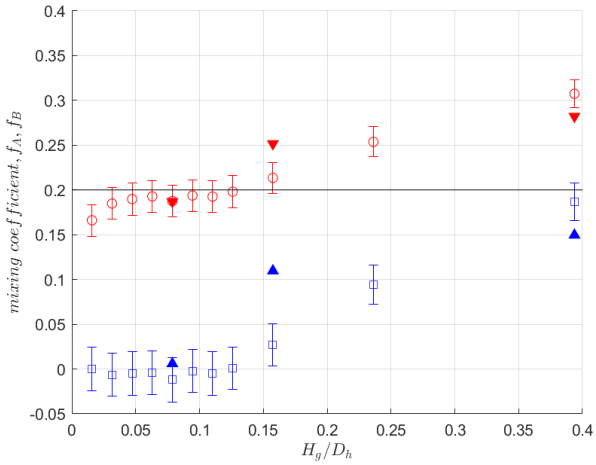

Fig. 12 Comparison of mixing coefficients f_A and f_B of Re = [6, 10]×10^4 based on the dye concentration and the SVD of the PIV data; blue square: f_A based on the dye concentration, red circle: f_B based on the dye concentration, blue triangle: f_A based on the SVD of the PIV data, red downward triangle: f_B based on the SVD of the PIV data.

4 Coherent Flow Structures within the Gap

As shown in Fig. 6, the instantaneous flow in the channels are dominated by the presence of coherent structures. PIV measurements within the gap were used to further characterize these coherent structures, and SVD is utilized in an attempt to determine how these structures contribute to the inter-channel mixing. As mention in section 2.3, the PIV data sets at the three FOV locations were obtained independently rather than si-

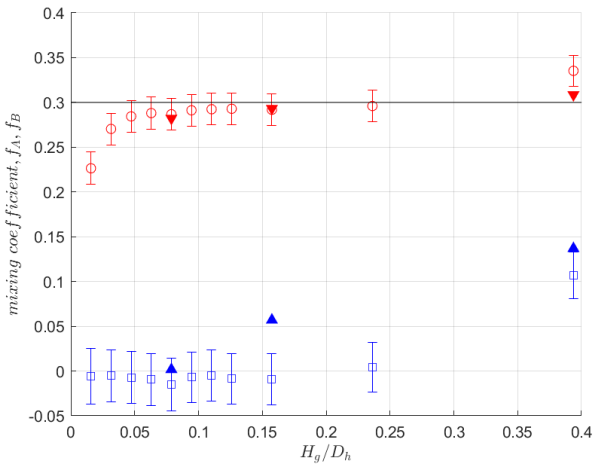

Fig. 13 Comparison of mixing coefficients f_A and f_B of Re = [40, 100] $\times 10^4$ based on the dye concentration and the SVD of the PIV data; blue square: f_A based on the dye concentration, red circle: f_B based on the dye concentration, blue triangle: f_A based on the SVD of the PIV data, red downward triangle: f_B based on the SVD of the PIV data.

multaneously. As such, the instantaneous PIV data cannot simply be integrated to estimate $\dot{m}$ and a spectral decomposition method is needed.

4.1 Frequency Analysis of the Coherent Structures

The vortex shedding is characterized with a single dominant frequency based on $u(i,j,k)$ and $v(i,j,k)$, which are the transverse and vertical velocity components, respectively. (Here i and j are 2D spatial axis indices, and k is the time index.) Next, the peak frequency f_p of each velocity component at every position (i,j) is defined as the frequency component that has the maximum amplitude:

$$f_p^{(u)}(i,j) = \arg\max_f \left|\mathcal{F}_k\{u(i,j,k)\}(f)\right|, \tag{17}$$

$$f_p^{(v)}(i,j) = \arg\max_f \left|\mathcal{F}_k\{v(i,j,k)\}(f)\right|, \tag{18}$$

where $\mathcal{F}_k\{\cdot\}$ denotes 1D Discrete-Time Fourier Transform (DTFT), and f is the frequency. Finally, the dominant peak frequency f_d is defined as the most frequent peak frequency.

$$f_d = \text{mode}[\boldsymbol{f}_p], \tag{19}$$

where $\boldsymbol{f}_p = \{f | f = f_p^{(u)}(i,j)$ or $f = f_p^{(v)}(i,j)$ for all $1 \le i \le N_y$ and $1 \le j \le N_x\}$. Now the Strouhal number can be defined as:

$$\text{St} = \frac{f_d W_g}{V}, \tag{20}$$

where f_d is the dominant peak frequency defined in Eqn. (19), the gap width W_g is taken as the characteristic length, and V is the characteristic flow velocity chosen as V the average velocity at the channel inlets.

The vortex shedding behavior in unbalanced flow was less periodic, with fluctuations distributed over a wide range of frequencies. However, for the balanced flow cases a dominant frequency is clearly definable and presented in Fig. 14. The Strouhal number is not strongly dependent on the inlet Reynolds number, but it is sensitive to the gap width ratio H_d/W_g.

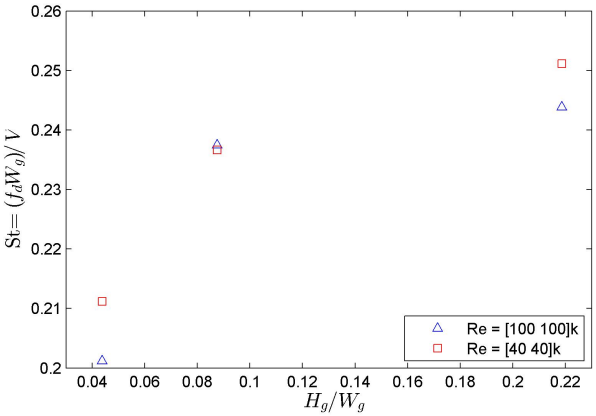

Fig. 14 Strouhal number of the balanced flows Re = [10 10]$\times 10^4$ (blue triangle) and Re=[4 4]$\times 10^4$ (red square) plotted against the gap height/gap width ratio.

There are only a few studies exploring in detail the flow geometry discussed in this paper; however, Meyer and Rehme [1] present the most significant data set for a similar geometry. A comparison to present study is not straightforward, but for a simple comparison definition from Eq. (20) can be used and for the clearest cases in which we can find the relevant information ([1] p. 295 case with 77 mm gap, 21.5 m/s average velocity and frequency peak of 68 Hz). Their data suggest a $St \approx 0.25$ when the gap height to width ratio is 0.13, corresponding to $H_g/W_g = 0.25$. This appears to be in reasonable agreement with data presented in Fig. 14.

4.2 Singular Value Decomposition of the Flow Fields

We now employ Singular Value Decomposition [20] to analyze the PIV flow fields in the gap. The data is represented by a matrix $A \in \mathbb{R}^{M\times N}$ that has spatial domain as rows and time domain as columns. The SVD theorem states that there exist matrices $\mathbf{L}$, $\boldsymbol{\Sigma}$, and $\mathbf{R}$ such that

$$\mathbf{A} = \mathbf{L}\boldsymbol{\Sigma}\mathbf{R}^{\mathrm{T}}, \tag{21}$$

$\mathbf{L} = [l_1\, l_2\, \cdots\, l_M]$ and $\mathbf{R} = [r_1\, r_2\, \cdots\, r_N]$ are orthogonal matrices, *i.e.*, all its columns are orthonormal to each other, and $\boldsymbol{\Sigma}$ is a diagonal matrix with all its diagonal elements greater than or equal to zero. The diagonal elements of $\boldsymbol{\Sigma}$ are sorted in descending order, $\sigma_1 \geq \sigma_2 \geq \cdots \geq \sigma_L \geq 0$, where L is the minimum between M and N.

The most energetic temporal basis vector R_1 which corresponds to σ_1 is obtained by solving the following optimization problem:

$$r_1 = \arg\max_{r_1} \frac{||\mathbf{A}r_1||_2}{||r_1||_2} = \arg\max_{r_1} \frac{r_1^{\mathrm{T}}\mathbf{A}^{\mathrm{T}}\mathbf{A}r_1}{r_1^{\mathrm{T}}r_1}, \tag{22}$$

Since every column of $\mathbf{R}$ is orthonormal to each other, the second most energetic temporal basis vector r_2 can be obtained by imposing an additional constraint:

$$\begin{aligned} r_2 = \arg\max_{r_2} \frac{||\mathbf{A}r_2||_2}{||r_2||_2} \quad &= \arg\max_{r_2} \frac{r_2^{\mathrm{T}}\mathbf{A}^{\mathrm{T}}\mathbf{A}r_2}{r_2^{\mathrm{T}}r_2}. \\ \text{such that } r_1^{\mathrm{T}}r_2 = 0 \quad &\text{such that } r_1^{\mathrm{T}}r_2 = 0 \end{aligned} \tag{23}$$

The most energetic spatial basis vector l_1 can be obtained by transposing the data matrix A:

$$l_1 = \arg\max_{l_1} \frac{||\mathbf{A}^{\mathrm{T}}l_1||_2}{||l_1||_2} = \arg\max_{l_1} \frac{l_1^{\mathrm{T}}\mathbf{A}\mathbf{A}^{\mathrm{T}}l_1}{l_1^{\mathrm{T}}l_1}, \tag{24}$$

and $\mathbf{L}$ is the eigenvector matrix of $\mathbf{A}\mathbf{A}^{\mathrm{T}}$.

Prior to the SVD, the mean value of $u \in \mathbb{R}^{N_y \times N_x \times N_t}$ and $v \in \mathbb{R}^{N_y \times N_x \times N_t}$ is substracted:

$$u'(i,j,k) = u(i,j,k) - \bar{u}(i,j), \tag{25}$$

$$v'(i,j,k) = v(i,j,k) - \bar{v}(i,j), \tag{26}$$

where $\bar{u}$ and $\bar{v}$ are the sample mean of u and v, respectively. Next, data u and v are reordered into two dimensional matrix $\mathbf{A}_u \in \mathbb{R}^{2N_y N_x \times N_t}$.

The resulting column vector of $\mathbf{L}$ (left singular vector) and $\mathbf{R}$ (right singular vector) represent the spatial and temporal basis vector, respectively. The analysis is completed by sorting the column vectors of $\mathbf{L}$ into two-dimensional velocity fields.

Evaluating the eight most energetic modes for each of the three PIV FOVs shows that in most cases the energy sum of these eight modes exceed 90 % of the total energy. To illustrate the SVD decomposed velocity fields, the results for the case of balanced flow with Re = [10, 10]$\times 10^4$ with a 10 mm gap are first presented. Fig. 15 presents the time-averaged flow fields for each FOV, along with the first two modes from the SVD. As the flow condition is symmetric, one can expect the corresponding averaged flow fields and SVD modes to also be symmetric; this is generally the case. Fig. 16 presents the third and fourth modes, along with the spectra of first four singular vectors. The frequency is normalized by the dominant frequency, and the spectral peaks occur at or very near multiples of f_d, although close examination of the peaks sometimes revealed two closely spaced frequency maxima, as discussed in [17]. Fig. 17 shows the normalized singular values and their energy proportions of the first eight modes. The first two modes contain most of the energy, and this is typical for all the balanced cases. Similar results for the other balanced cases are presented in [17].

Figs. 18, 19, 20 present the mean velocity field, SVD of the first four spatial modes, the spectra of first four singular vectors, and the energy distributions for the unbalanced case of Re=[6, 10]$\times 10^4$ with a 20 mm gap. The time-averaged flow fields show a mean lateral flow across the gap. The SVD results for unbalanced flow fields are no longer symmetric, as expected. The temporal singular vectors do not have a strong harmonic content compared to those for the balanced cases, as the coherent structures are much less periodic. Most of the energy is, once again, contained in the first two periodic modes. Similar results for the other unbalanced cases are presented in [17].

5 Estimation of the Mixing Coefficients Based on PIV Data

The inter-channel mixing coefficients are now estimated using the mean velocity fields and SVD in order to identify how the strongest periodic motions contribute to the overall mass transfer between the two channels. Mixing rates estimated based on the SVD analysis will also be compared to mixing rates measured from the tracer dye transport. The main assumption employed is that the mixing process can be linearly decomposed and then superimposed. If this is the case, SVD data can be used to compute steady and dynamic mixing coefficients, $f_A^{(s)}$ and $f_A^{(d)}$ that will sum to the total mixing coefficient determined in Section 3.

$$f_A = f_A^{(s)} + f_A^{(d)}, \tag{27}$$

$$f_B = f_B^{(s)} + f_B^{(d)}, \tag{28}$$

Recall that not all coherent modes will contribute to the mass transfer between two channels, as discussed above. Because the majority of the flow energy is in the first two modes, only these two modes will be considered for the mixing analysis. Thus, the higher modes are considered to be localized turbulence, and assumed to not significantly contribute to the mass transfer. Finally, to determine the overall mixing coefficient, additional assumptions are needed about the portions of

the flow in the gap that were not captured by the PIV imaging.

5.1 Approximation of the Non-Visualized Average Flow in the Gap

As shown in Fig. 4, there are portions of the gap flow that are not captured by the PIV imaging. In order to estimate the mean flow across the entire gap, one must account for this non-visualized flow. Examination of the time averaged flow fields suggest that most of the transverse flow at the edges of the gap occurs at the start (inflow) and the end (outflow) (FOVs 1 and 3), while the average flow converges to a near upwards flow near the middle of the gap (FOV 2) Fig. 15a. Hence, it is assumed that the flows in the non-visualized portions of the gap are similar to that of FOV 2 (the middle field of view), and factor β is introduced:

$$\beta_p = \begin{cases} 1 & \text{if } p = 1 \text{ or } 3, \\ 2.11 & \text{if } p = 2, \end{cases} \tag{29}$$

where the factor 2.11 accounts for the inferred area of the gap flow, which is 1.11 times the area of FOV2.

5.2 Center-plane *versus* Average Flow Velocities in the Gap

The PIV data is collected at the gap center-plane, which is likely a higher velocity than the bulk velocity. While the actual flow from in this case is transient and spatially non-uniform, one could approximate this flow as 2D channel flow for which the center plane velocity is in proportion to the average velocity with a ratio defined as $\theta(Re_{gap})$. In the case of a unidirectional laminar gap flow, $\theta(Re_{gap})= 2/3$ and for a fully turbulent flow, the values are a function of Reynolds number [21] with ratios increasing with Reynolds number from 0.88 to 0.90. The computed fluxes are reduced based on the mid-plane velocity through application of $\theta(Re_{gap})$. As the flow is unsteady and non-unidirectional and value is needed in gap entrance/exit region, for simplicity $\theta(Re_{gap})$ is approximated to be a constant 0.85. Application of this correction would reduce the estimated mixing coefficients by 15%.

Figures1.pdf Figures1.pdf

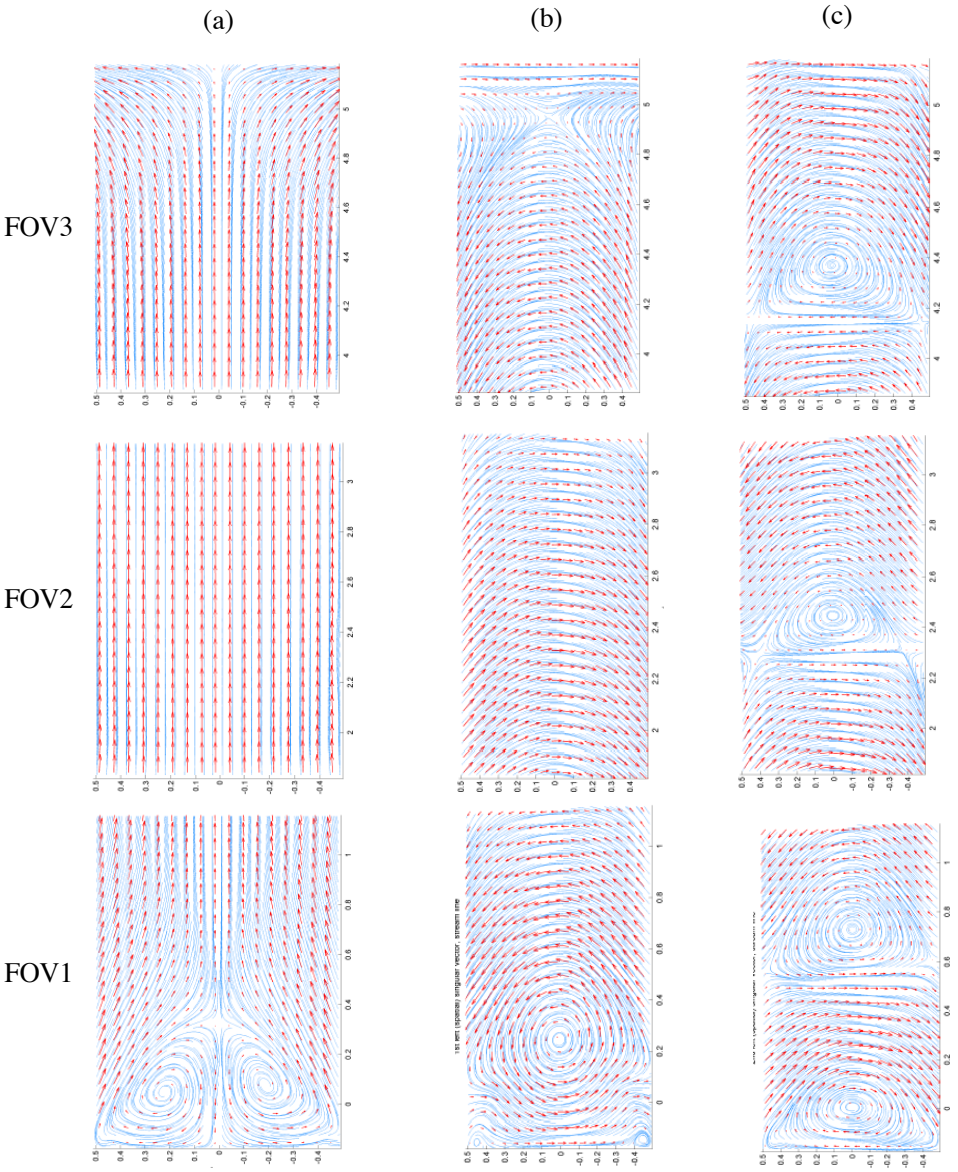

Fig. 15 The (a) time averaged velocity field of Re = [10 10]×10^4, H_g = 10 mm (H_g/D_h = 0.079); the three FOVs are shown; the singular vectors of the first (b) and the second (c) spatial modes are also shown; red arrows indicate velocity vectors, and blue lines indicate streamlines.

Figures2.pdf Figures2.pdf

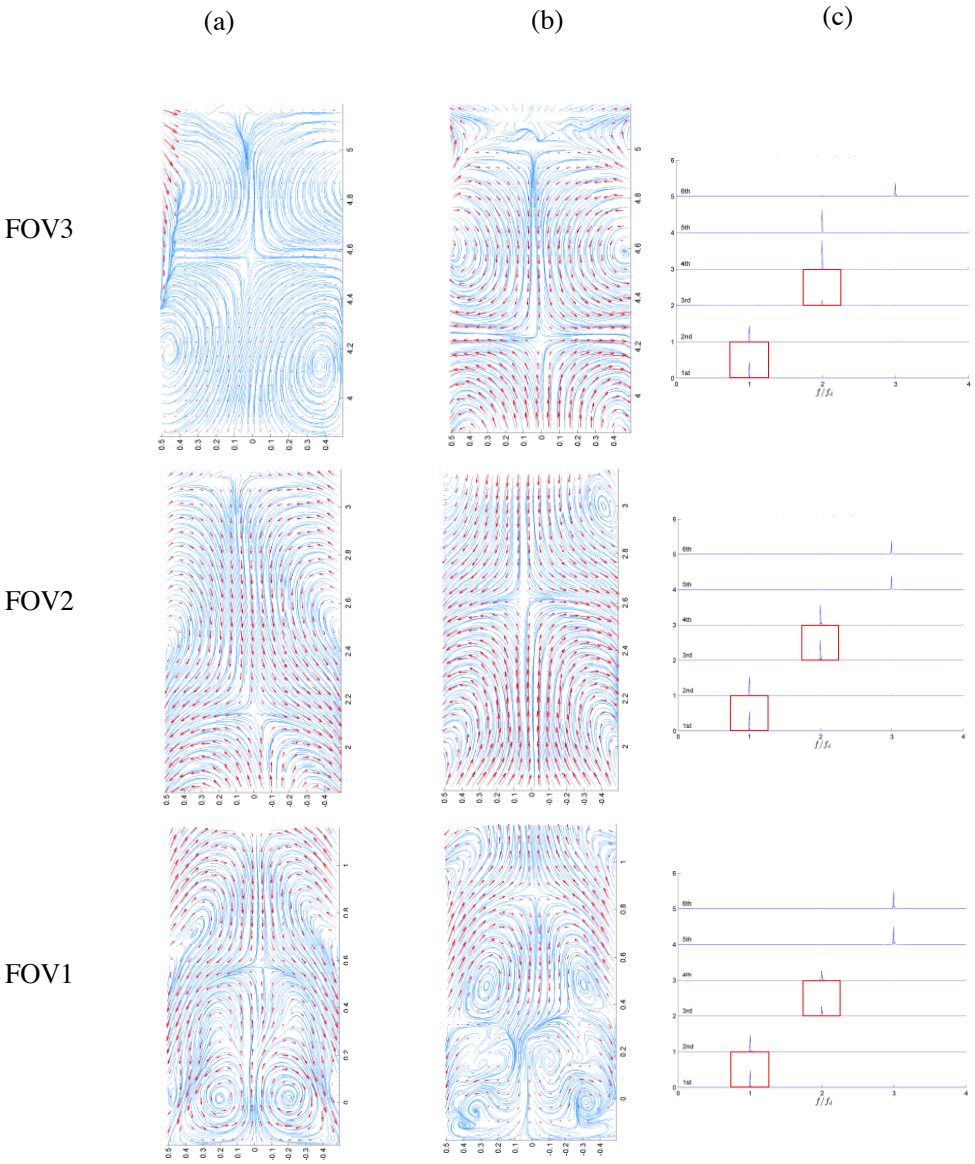

Fig. 16 The singular vectors of the (a) third and the (b) forth spatial modes for Re = [10 10]×10^4, H_g = 10 mm (H_g/D_h = 0.079); red arrows indicate velocity vectors, and blue lines indicate streamlines; shown in column (c) are the temporal power spectral densities of the first four right singular vectors; the red squares in (c) show the first and third modes.

Figures3.pdf Figures3.pdf

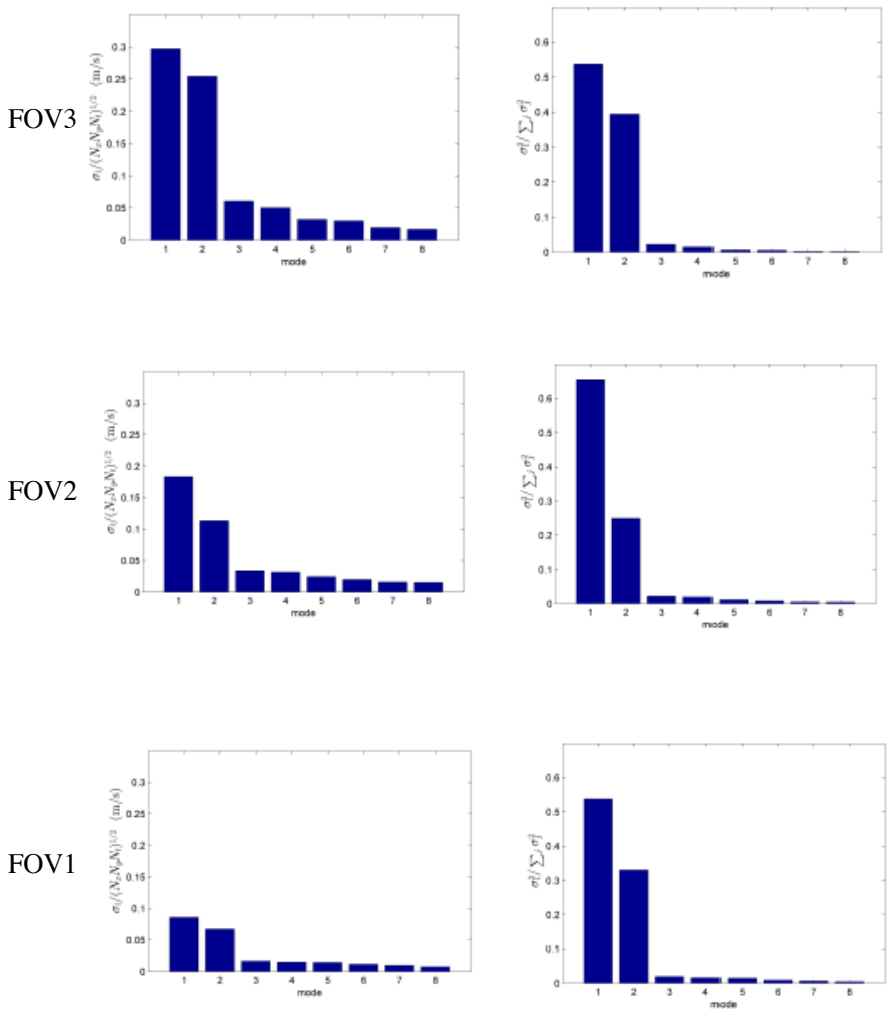

Fig. 17 The normalized singular values (a) and their energy proportions (b) of the first eight modes for Re=[10 10]$\times 10^4$, H_g = 10 mm (H_g/D_h = 0.079).

Figures4.pdf Figures4.pdf

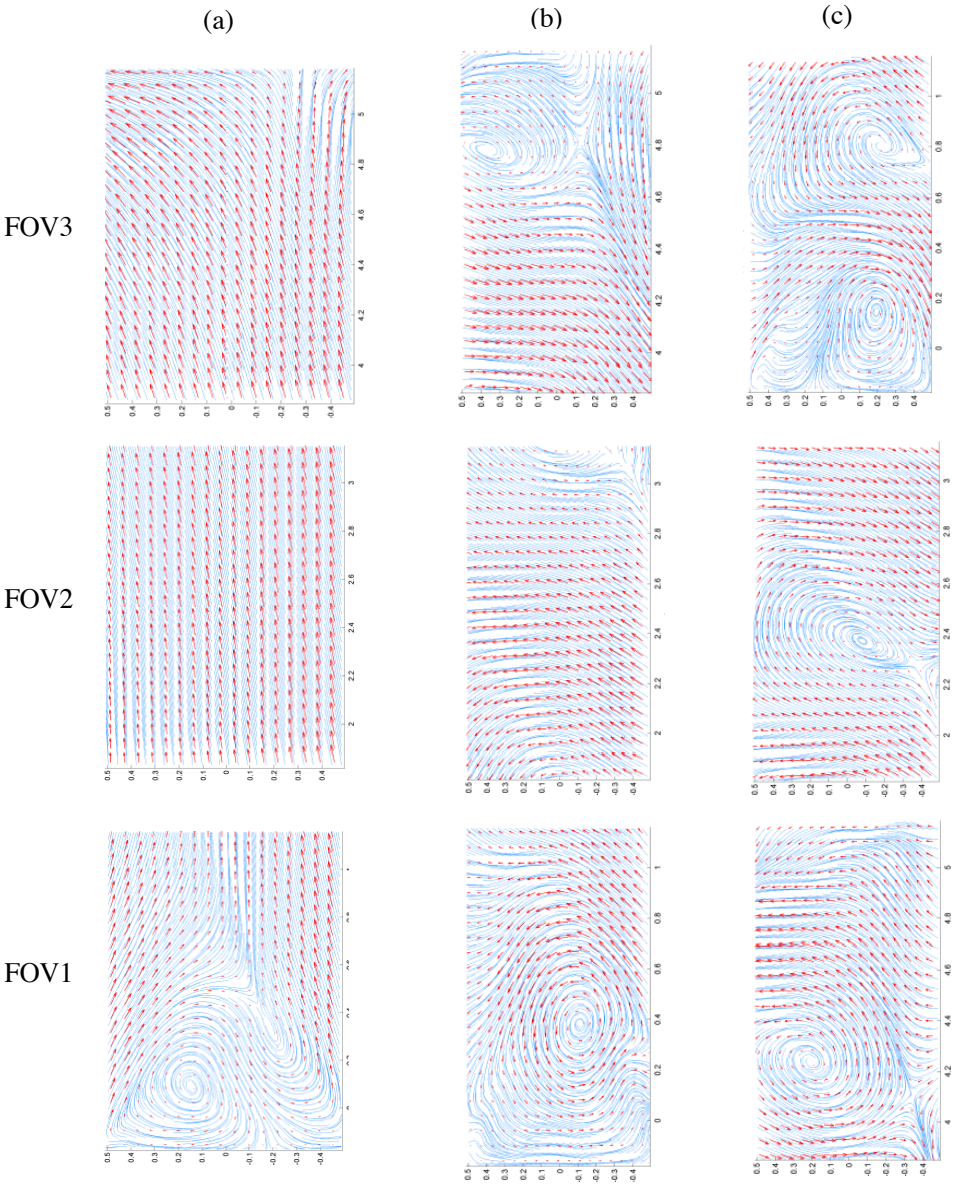

Fig. 18 The (a) time averaged velocity field of Re = [6 10]×10^4, H_g = 20 mm (H_g/D_h = 0.157); the three FOVs are shown; the singular vectors of the first (b) and the second (c) spatial modes are also shown; red arrows indicate velocity vectors, and blue lines indicate streamlines.

Figures5.pdf Figures5.pdf

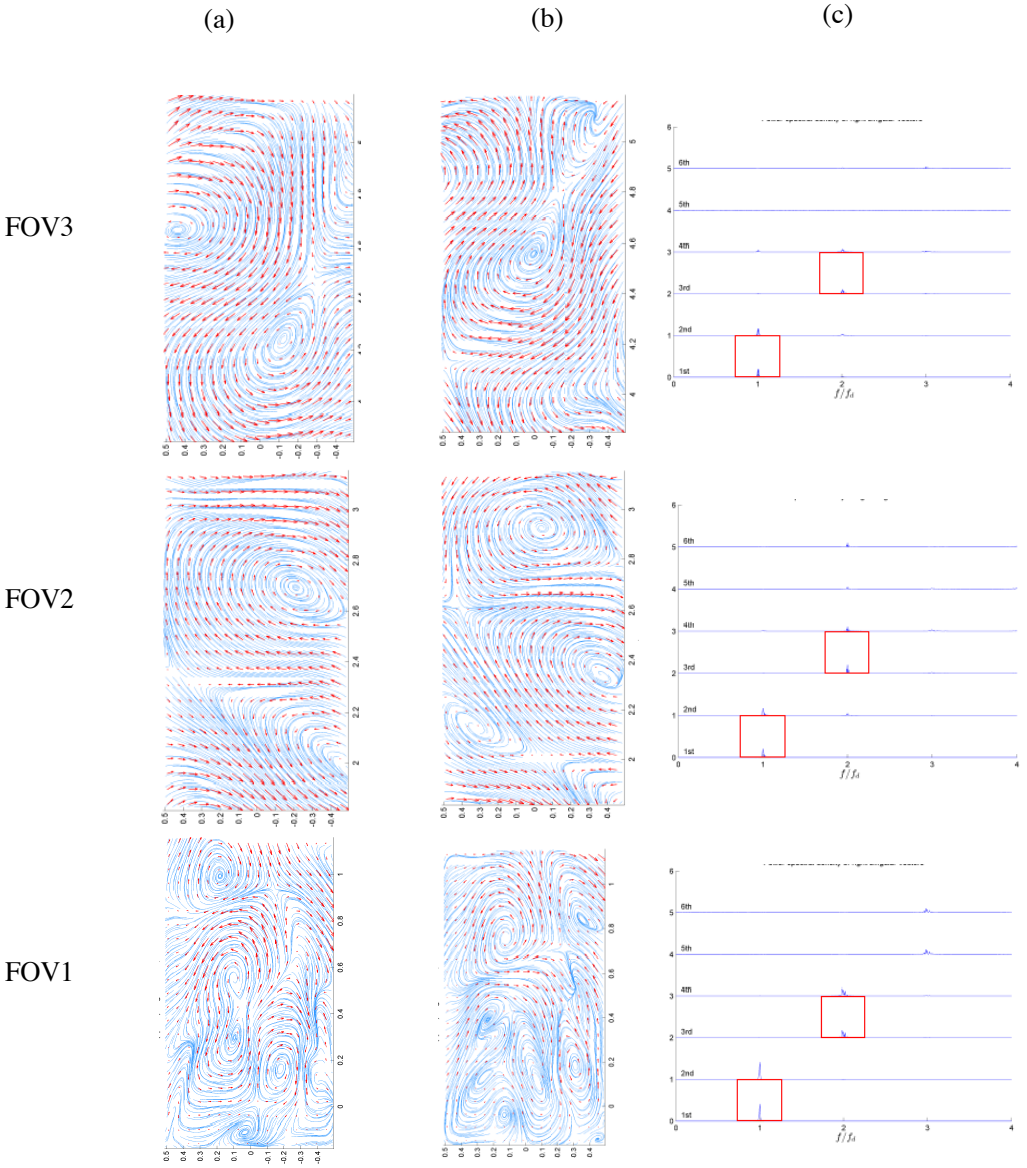

Fig. 19 The singular vectors of the (a) third and the (b) forth spatial modes for Re=[6 10]$\times 10^4$, H_g = 20 mm (H_g/D_h = 0.157); red arrows indicate velocity vectors, and blue lines indicate streamlines; shown in column (c) are the temporal power spectral densities of the first four right singular vectors; the red squares in (c) show the first and third modes.

Figures6.pdf Figures6.pdf

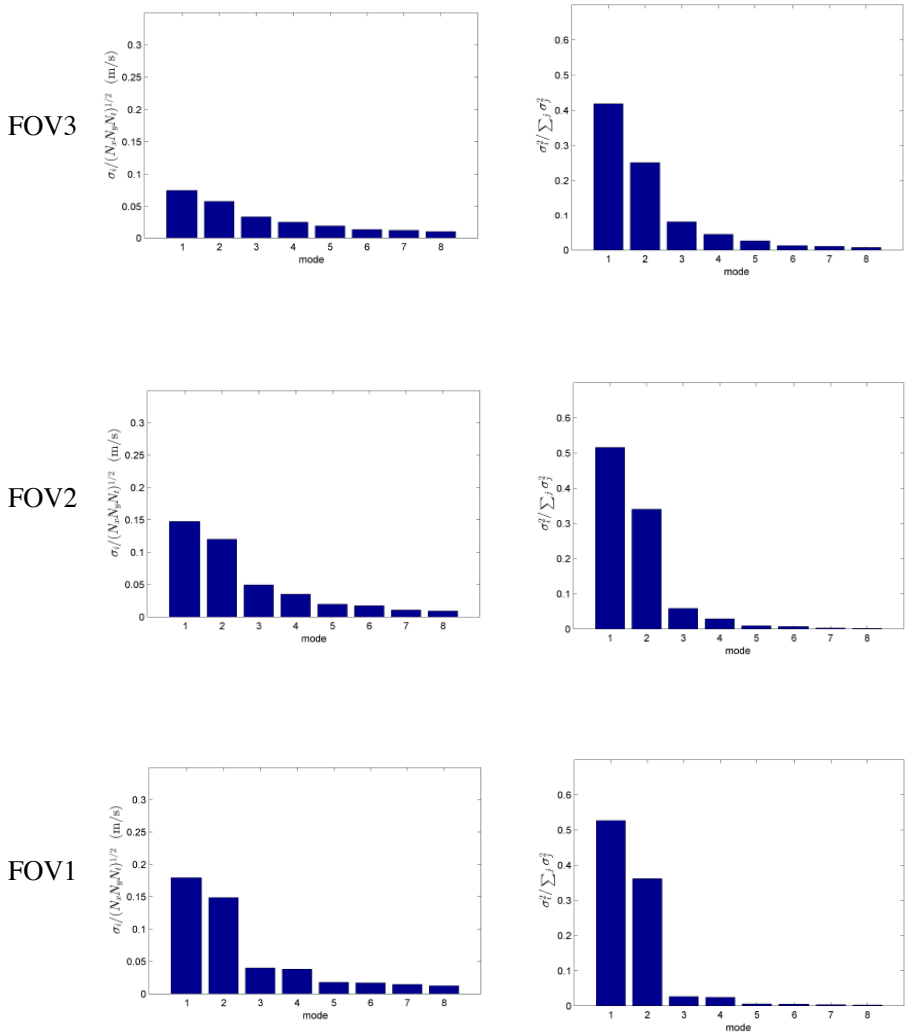

Fig. 20 The normalized singular values (a) and their energy proportions (b) of the first eight modes for Re = [6 10]$\times 10^4$, H_g = 20 mm (H_g/D_h = 0.157).

5.3 Estimation of the Steady Mixing Across the Gap

Taking a control volume around the boundary of the gap, the transverse flow from side edges of the gap must also be considered. Let $\bar{F}_A$ and $\bar{F}_B$ be the total steady volume flow rates at the side edges of the gap adjacent to Channel A and Channel B, respectively.

$$\bar{F}_A = H_g \int_0^{L_g} \theta(Re_{gap})\bar{u}(\mathrm{y}, W_g/2)\mathrm{dy}, \tag{30}$$

$$\bar{F}_B = H_g \int_0^{L_g} \theta(Re_{gap})\bar{u}(\mathrm{y}, -W_g/2)\mathrm{dy}, \tag{31}$$

where $\bar{u}$ is the time averaged transverse velocity, H_g is the gap height, L_g is the gap vertical length, W_g is the gap width. (Note: x and y are the local coordinates with the origin at the center bottom of the gap, while f_A and f_B are the mixing coefficients.)

After discretization, the corrected flow rates including the entire area of the gap are given by:

$$\bar{F}_A = H_g \sum_{p=1}^{3} \left(\beta_p \sum_{i=1}^{N_\mathrm{y}} \theta(Re_{gap})\bar{u}^{(p)}(i,1)\Delta\mathrm{y} \right), \tag{32}$$

$$\bar{F}_B = H_g \sum_{p=1}^{3} \left(\beta_p \sum_{i=1}^{N_\mathrm{y}} \theta(Re_{gap})\bar{u}^{(p)}(i,N_x)\Delta\mathrm{y} \right), \tag{33}$$

where p is the FOV index, i is the y index, N_y and N_x are the total number of pixels in y axis and x axis, respectively. $\bar{u}^{(p)}(i,j)$ is the time-average of the transverse velocity u at (i,j) location in FOV p.

The mass conservation in a control volume encompassing the entire gap requires $\bar{F}_A = \bar{F}_B$. Uncertainties in the PIV data result in vector fields that do not completely satisfy mass conservation at every time step, with errors typically less than $\pm 2.5\%$ of the total flux. Hence, using the average value of $\bar{F}_A$ and $\bar{F}_B$ to compute the steady mixing coefficients:

$$\begin{cases} f_A^{(s)} = \dfrac{|\bar{F}_A + \bar{F}_B|}{2\bar{V}_\mathrm{Ai}},\ f_B^{(s)} = 0 & \text{if } \bar{F}_A + \bar{F}_B < 0 \\ f_A^{(s)} = 0,\ f_B^{(s)} = \dfrac{|\bar{F}_A + \bar{F}_B|}{2\bar{V}_\mathrm{Bi}} & \text{if } \bar{F}_A + \bar{F}_B \geq 0, \end{cases} \tag{34}$$

where $\bar{V}_\mathrm{Ai}$ and $\bar{V}_\mathrm{Bi}$ are the nominal volume flow rates at the inlet of Channel A and Channel B, respectively.

5.4 Mixing As a Result of the Coherent Motions

The mixing due to the coherent structures is periodic, and flow should be analyzed as it moves in both directions (*i.e.* Channel A to Channel B and Channel B to Channel A.) Thus, instead of integrating the transverse flow rate, the flow must first be divided into portions that enter and exit the gap, and then integrated separately. Next, the absolute volume flow rate can be calculated after the time-averaged velocity is subtracted.

$$F_{A_\mathrm{in}}(t) = -H_g \int_0^{L_g} \min\{u'(\mathrm{y}, W_g/2, t),\, 0\}\,\mathrm{dy}, \tag{35}$$

$$F_{A_\mathrm{out}}(t) = H_g \int_0^{L_g} \max\{u'(\mathrm{y}, W_g/2, t),\, 0\}\,\mathrm{dy}, \tag{36}$$

$$F_{B_\mathrm{in}}(t) = H_g \int_0^{L_g} \max\{u'(\mathrm{y}, -W_g/2, t),\, 0\}\,\mathrm{dy}, \tag{37}$$

$$F_{B_\mathrm{out}}(t) = -H_g \int_0^{L_g} \min\{u'(\mathrm{y}, -W_g/2, t),\, 0\}\,\mathrm{dy}. \tag{38}$$

Here, $\min\{\cdot, 0\}$ and $\max\{\cdot, 0\}$ are applied to the flow u' to shift and collect entering and exiting flows separately (*e.g.* when u' is > 0, $\min\{u', 0\}$ returns 0 whereas $-u'$ would return $-u'$).

Note that all $F_{(A|B)_{(\mathrm{in}|\mathrm{out})}}$ are defined as absolute values. Discretizing Eqn. (35) to (38) for p^{th} FOV yields

$$F_{A_\mathrm{in}}^{(p)}(k) = -H_g \sum_{i=1}^{N_\mathrm{y}} \min\left\{u'^{(p)}(i,1,k),\, 0\right\}\Delta\mathrm{y}, \tag{39}$$

$$F_{A_\mathrm{out}}^{(p)}(k) = H_g \sum_{i=1}^{N_\mathrm{y}} \max\left\{u'^{(p)}(i,1,k),\, 0\right\}\Delta\mathrm{y}, \tag{40}$$

$$F_{B_\mathrm{in}}^{(p)}(k) = H_g \sum_{i=1}^{N_\mathrm{y}} \max\left\{u'^{(p)}(i,N_x,k),\, 0\right\}\Delta\mathrm{y}, \tag{41}$$

$$F_{B_\mathrm{out}}^{(p)}(k) = -H_g \sum_{i=1}^{N_\mathrm{y}} \min\left\{u'^{(p)}(i,N_x,k),\, 0\right\}\Delta\mathrm{y}. \tag{42}$$

For estimating the coherent mixing, two additional assumptions are needed. First, that there is no re-entry of flow into the gap, *i.e.*, $F_{A_\mathrm{in}}^{(p)}(t)$ is only from the source of Channel A, and $F_{B_\mathrm{in}}^{(p)}(t)$ is only from Channel B. Second, for each FOV, the fluid is fully mixed by the local turbulence so that the composition of outgoing flow is uniformly proportional to the flow rates entering from Channels A and B. Then, the flow rates between Channels A and B can be taken as:

$$F_{A\to B}^{(p)}(k) = \theta(Re_{gap}) \left(\frac{F_{A_\mathrm{in}}^{(p)}(k)}{F_{A_\mathrm{in}}^{(p)}(k) + F_{B_\mathrm{in}}^{(p)}(k)} \right) F_{B_\mathrm{out}}^{(p)}(k), \tag{43}$$

$$F_{B\to A}^{(p)}(k) = \theta(Re_{gap}) \left(\frac{F_{B_\mathrm{in}}^{(p)}(k)}{F_{A_\mathrm{in}}^{(p)}(k) + F_{B_\mathrm{in}}^{(p)}(k)} \right) F_{A_\mathrm{out}}^{(p)}(k). \tag{44}$$

Eqn. (43) and (44) are time dependent. The SVD decomposes the data into spatial (left singular vectors)

and temporal (right singular vectors) bases along with their intensity (singular values). Using the SVD results, the time-averaged coherent mixing for each FOV can be estimated.

Denote $l^{(p,s)}$, $\sigma^{(p,s)}$, and $r^{(p,s)}$ as the left singular vector, the singular value, and the right singular vector of the s^{th} mode taken at p^{th} FOV. Let $\hat{u}^{(p,s)}_{(i,j)}$ be the reordered matrix of the transverse velocity part of the p^{th} FOV, s^{th} left singular vector,

$$\hat{u}^{(p,s)}_{(i,j)} = l^{(p,s)}(N_x N_y + N_x i + j), \tag{45}$$

where $l^{(p,s)}$ is the s^{th} left singular vector of p^{th} FOV data. Then, rewriting the centered transverse flow velocity of s^{th} mode $u'^{(p,s)}_{(i,j,k)}$ in terms of $\hat{u}^{(p,s)}_{(i,j)}$, singular value, and right singular vector,

$$u'^{(p,s)}_{(i,j,k)} = \hat{u}^{(p,s)}_{(i,j)} \sigma^{(p,s)} r^{(p,s)}_{(k)}. \tag{46}$$

In the right hand side of Eqn. 46, only $r^{(p,s)}_{(k)}$ depends on time. Hence, time-average of $u'^{(p,s)}_{(i,j,k)}$ is found by time-averaging $r^{(p,s)}_{(k)}$. However, just taking time-average of $r^{(p,s)}_{(k)}$ only yields zero. Therefore, $r^{(p,s)}_{(k)}$ must be split into a positive and negative phase,

$$\left\{r^{(p,s)}\right\}^{+} = \frac{\sum_{k=1}^{N_k} \max\{r^{(p,s)}_{(k)},\ 0\}}{N_k}, \tag{47}$$

$$\left\{r^{(p,s)}\right\}^{-} = -\frac{\sum_{k=1}^{N_k} \min\{r^{(p,s)}_{(k)},\ 0\}}{N_k}, \tag{48}$$

where N_k is the total number of the temporal sampling points. One can see that $\left\{r^{(p,s)}\right\}^{+} = \left\{r^{(p,s)}\right\}^{-}$ as time-average of $r^{(p,s)}_{(k)}$ is zero. Using Eqn. (47), the absolute valued time-average flow rate is given by

$$\{F^{(p,s)}_{A_{\text{in}}}\}^{+} = -H_g \left(\sum_{i=1}^{N_i} \min\{\hat{u}^{(p,s)}_{(i,1)},\ 0\}\, \Delta y\right) \sigma^{(p,s)} \{r^{(p,s)}_{(k)}\}^{+}, \tag{49}$$

$$\{F^{(p,s)}_{A_{\text{out}}}\}^{+} = H_g \left(\sum_{i=1}^{N_i} \max\{\hat{u}^{(p,s)}_{(i,1)},\ 0\}\, \Delta y\right) \sigma^{(p,s)} \{r^{(p,s)}_{(k)}\}^{+}, \tag{50}$$

$$\{F^{(p,s)}_{B_{\text{in}}}\}^{+} = H_g \left(\sum_{i=1}^{N_i} \max\{\hat{u}^{(p,s)}_{(i,N_x)},\ 0\}\, \Delta y\right) \sigma^{(p,s)} \{r^{(p,s)}_{(k)}\}^{+}, \tag{51}$$

$$\{F^{(p,s)}_{B_{\text{out}}}\}^{+} = -H_g \left(\sum_{i=1}^{N_i} \min\{\hat{u}^{(p,s)}_{(i,N_x)},\ 0\}\, \Delta y\right) \sigma^{(p,s)} \{r^{(p,s)}_{(k)}\}^{+}, \tag{52}$$

$$\left\{F^{(p,s)}_{A_{\text{in}}}\right\}^{-} = \left\{F^{(p,s)}_{A_{\text{out}}}\right\}^{+}, \tag{53}$$

$$\left\{F^{(p,s)}_{A_{\text{out}}}\right\}^{-} = \left\{F^{(p,s)}_{A_{\text{in}}}\right\}^{+}, \tag{54}$$

$$\left\{F^{(p,s)}_{B_{\text{in}}}\right\}^{-} = \left\{F^{(p,s)}_{B_{\text{out}}}\right\}^{+}, \tag{55}$$

$$\left\{F^{(p,s)}_{B_{\text{out}}}\right\}^{-} = \left\{F^{(p,s)}_{B_{\text{in}}}\right\}^{+}. \tag{56}$$

Applying Eqn. (49)-(56) to Eqn. (43) and (44), and multiplying by θ to correct centerline to mean velocity ratio, the time-averaged dynamic (or coherent) mixing coefficients is given by:

$$f^{(d)}_{A} = \theta(Re_{gap}) \sum_{p=1}^{3} \sum_{s=1}^{N_s} \frac{\left\{F^{(p)}_{A\to B}\right\}^{+} + \left\{F^{(p)}_{B\to A}\right\}^{-}}{\bar{V}_{Ai}}, \tag{57}$$

$$f^{(d)}_{B} = \theta(Re_{gap}) \sum_{p=1}^{3} \sum_{s=1}^{N_s} \frac{\left\{F^{(p)}_{B\to A}\right\}^{+} + \left\{F^{(p)}_{A\to B}\right\}^{-}}{\bar{V}_{Bi}}, \tag{58}$$

where

$$\left\{F^{(p)}_{A\to B}\right\}^{*} = \left(\frac{\left\{F^{(p)}_{A_{\text{in}}}\right\}^{*}}{\left\{F^{(p)}_{A_{\text{in}}}\right\}^{*} + \left\{F^{(p)}_{B_{\text{in}}}\right\}^{*}}\right) \left\{F^{(p)}_{B_{\text{out}}}\right\}^{*}, \tag{59}$$

$$\left\{F^{(p)}_{B\to A}\right\}^{*} = \left(\frac{\left\{F^{(p)}_{B_{\text{in}}}\right\}^{*}}{\left\{F^{(p)}_{A_{\text{in}}}\right\}^{*} + \left\{F^{(p)}_{B_{\text{in}}}\right\}^{*}}\right) \left\{F^{(p)}_{A_{\text{out}}}\right\}^{*}, \tag{60}$$

where $*$ denotes the sign, $+$ or $-$. However, the dynamic coefficients thus defined do not account for contribution of non-visualized flow. Hence, eq. 57 and 58 require a correction that will be discussed next.

5.5 Approximation of the Non-Visualized Unsteady Flow in the Gap

The unsteady flow that may occur at the top and bottom of the FOVs must also be considered. This is 5 to 15% of the total unsteady volume flow rate for balanced flow conditions, and up to to 30% for unbalanced flow. Estimating those sources of vertical flows is essential to estimate the coherent mixing. Assuming that the unknown vertical volume flux is proportional to the known lateral flow between Channel A and B that is observable in any FOV. Let $F^{(p,s)}_{\text{in}}$ and $F^{(p,s)}_{\text{out}}$ be the total flow rates of the s^{th} singular mode incoming/outgoing from both sides of the gap in p^{th} FOV, respectively.

$$F^{(p,s)}_{\text{in}} = F^{(p,s)}_{A_{\text{in}}} + F^{(p,s)}_{B_{\text{in}}}, \tag{61}$$

$$F^{(p,s)}_{\text{out}} = F^{(p,s)}_{A_{\text{out}}} + F^{(p,s)}_{B_{\text{out}}}, \tag{62}$$

Then, the corrected flow rates can be taken as: If $F^{(p,s)}_{\text{in}} > F^{(p,s)}_{\text{out}}$

$$\begin{cases} \widetilde{F}^{(p,s)}_{A_{\text{in}}} = F^{(p,s)}_{A_{\text{in}}} \\ \widetilde{F}^{(p,s)}_{B_{\text{in}}} = F^{(p,s)}_{B_{\text{in}}} \\ \widetilde{F}^{(p,s)}_{A_{\text{out}}} = F^{(p,s)}_{A_{\text{out}}} + \left(F^{(p,s)}_{\text{in}} - F^{(p,s)}_{\text{out}}\right) \dfrac{F^{(p,s)}_{A_{\text{in}}}}{F^{(p,s)}_{\text{in}}} \\ \widetilde{F}^{(p,s)}_{B_{\text{out}}} = F^{(p,s)}_{B_{\text{out}}} + \left(F^{(p,s)}_{\text{in}} - F^{(p,s)}_{\text{out}}\right) \dfrac{F^{(p,s)}_{B_{\text{in}}}}{F^{(p,s)}_{\text{in}}} \end{cases}, \tag{63}$$

otherwise

$$\begin{cases} \widetilde{F}_{A_{\text{in}}}^{(p,s)} = F_{A_{\text{in}}}^{(p,s)} + \left(F_{\text{out}}^{(p,s)} - F_{\text{in}}^{(p,s)}\right) \dfrac{F_{A_{\text{out}}}^{(p,s)}}{F_{\text{out}}^{(p,s)}} \\ \widetilde{F}_{B_{\text{in}}}^{(p,s)} = F_{B_{\text{in}}}^{(p,s)} + \left(F_{\text{out}}^{(p,s)} - F_{\text{in}}^{(p,s)}\right) \dfrac{F_{B_{\text{out}}}^{(p,s)}}{F_{\text{out}}^{(p,s)}} \\ \widetilde{F}_{A_{\text{out}}}^{(p,s)} = F_{A_{\text{out}}}^{(p,s)} \\ \widetilde{F}_{B_{\text{out}}}^{(p,s)} = F_{B_{\text{out}}}^{(p,s)} \end{cases} . \tag{64}$$

The original flow rates in Eqn. (59)-(60) are substituted with the corrected flow rates in Eqn (63)-(64).

Owing to the assumption above to satisfy each FOV's mass conservation, some inflows and outflows could be partially double counted. To adjust for this possibility, the corrected flow rate is multiplied by a factor α_p to only consider the flow in and out for each FOV in terms of average values.

$$\alpha_p = \frac{\min\left\{F_{\text{in}}^{(p,s)}, F_{\text{out}}^{(p,s)}\right\}}{\max\left\{F_{\text{in}}^{(p,s)}, F_{\text{out}}^{(p,s)}\right\}}. \tag{65}$$

Finally, it is necessary to consider the effect of missing FOVs. While most of the steady mixing happened at the start and the end of the gap, mixing due to the coherent structures occurs more uniformly everywhere along the gap length. Hence, the areas of the two missing FOVs are evenly divided, and it is assumed the flow pattern in each missing FOV follows the flow pattern of the nearest known FOV. This is achieved in practice simply by multiplying the flow rate by the area ratio of each FOV:

$$\gamma_p = \begin{cases} 1.275 & \text{if p=1,} \\ 1.537 & \text{if p=2,} \\ 1.328 & \text{if p=3.} \end{cases} \tag{66}$$

Finally, computing the corrected coherent mixing coefficients:

$$f_A^{(d)} = \theta(Re_{gap}) \sum_{p=1}^{3} \left(\alpha_p \gamma_p \sum_{s=1}^{N_s} \frac{\left\{F_{A\to B}^{(p)}\right\}^+ + \left\{F_{B\to A}^{(p)}\right\}^-}{\bar{V}_{Ai}} \right), \tag{67}$$

$$f_B^{(d)} = \theta(Re_{gap}) \sum_{p=1}^{3} \left(\alpha_p \gamma_p \sum_{s=1}^{N_s} \frac{\left\{F_{B\to A}^{(p)}\right\}^+ + \left\{F_{A\to B}^{(p)}\right\}^-}{\bar{V}_{Bi}} \right). \tag{68}$$

5.6 Comparison of the Directly Measured and Computed Mixing Coefficients

After applying the analysis and necessary assumptions to the velocity field data described above, the mass transfer based on the flow field measurements and SVD can be computed and these results can be compared to the coefficients calculated based on the measured values from the tracer dye transport.

Table 1 presents computed and measured mixing coefficients for the balanced cases Re = [10 10]×10^4 and Re = [4 4]×10^4, each at the three gap heights of 10, 20, and 50 mm (H_g/D_h = 0.079, 0.157, and 0.393). These data (triangular symbols) are also shown in Figs. 8 and 9. For both Re = [10 10]×10^4 and Re = [4 4]×10^4, the measured and computed coefficients follow the same trends and are of the same order.

Table 2 show the steady, coherent, and total mixing coefficients for Re = [8 10]×10^4, Re = [6 10]×10^4, and Re = [4 10]×10^4, respectively for each the three gap heights of 10, 20, and 50 mm (H_g/D_h = 0.079, 0.157, and 0.393). It is observed that the steady mixing coefficients are almost constant in each flow condition regardless of the gap thickness, and the estimated steady mixing coefficients are mostly within 5 to 10% of the ideal steady mixing coefficients one can estimate by requiring that the flow is balanced by the outlet.

6 Conclusions

The mixing through a narrow gap was investigated based on both measurements of flow rates and dye concentrations at the channel inlets and outlets, as well as based on planar velocity fields within the mixing gap. The mixing coefficient was defined as a fraction of inlet flow transferred from one channel to the other. For balanced flows, over the finite range covered in present work, the mixing coefficients show a weak dependence on the Reynolds number when the gap ratio H_g/D_h is larger than 0.06. However, when $H_g/D_h < 0.06$, mixing coefficients show some deviation depending on the Reynolds number, albeit within the range of the 68 % confidence interval given the measurement uncertainty. There was no significant mixing within the uncertainty of the measurement for $H_g/D_h < 0.025$.

For unbalanced flow, the effect of the coherent structures on the mixing decreases as the flow becomes increasingly unbalanced leading to more mixing due to a simple pressure difference across the gap. And, as the unbalance increases, weaker large-scale structures are seen. SVD results confirmed that the energy of the coherent structures, based on the singular values, decreases. Also, the right singular values become less periodic as the velocity difference between two channels grows, as was shown in detail in [17].

The mixing coefficients were also estimated based on the SVD of the PIV data. While several assumptions

Table 1 Mixing coefficients based on SVD and dye tracer for the balanced cases. Recall, the total mixing coefficient, f, based on SVD is the sum of the steady and dynamic mixing coefficients, $f^{(s)}$ and $f^{(d)}$, respectively (eq. 27-28).

	Re = [4 4]$\times 10^{-4}$				Re = [10 10]$\times 10^{-4}$			
H_g [mm]	$f_A^{(s)}$ $f_B^{(s)}$	$f_A^{(d)}$ $f_B^{(d)}$	Tracer	$(f_A - x)/x$ $(f_B - y)/y$	$f_A^{(s)}$ $f_B^{(s)}$	$f_A^{(d)}$ $f_B^{(d)}$	Tracer	$(f_A - x)/x$ $(f_B - y)/y$
10	0.000	0.046	0.017	1.70	0.000	0.060	0.047	0.28
	0.003	0.046	0.018	1.69	0.002	0.060	0.049	0.27
20	0.000	0.134	0.128	0.05	0.000	0.133	0.134	0.00
	0.003	0.134	0.138	-0.01	0.003	0.133	0.137	0.00
50	0.000	0.317	0.323	-0.02	0.000	0.322	0.329	-0.02
	0.009	0.317	0.337	-0.03	0.014	0.322	0.330	0.02

Table 2 Mixing coefficients based on SVD and dye tracer for the unbalanced cases. Recall, the total mixing coefficient, f, based on SVD is the sum of the steady and dynamic mixing coefficients, $f^{(s)}$ and $f^{(d)}$, respectively (eq. 27-28).

	Re = [10 8]$\times 10^{-4}$				Re = [10 6]$\times 10^{-4}$				Re = [10 4]$\times 10^{-4}$			
H_g [mm]	$f_A^{(s)}$ $f_B^{(s)}$	$f_A^{(d)}$ $f_B^{(d)}$	Tracer	$(f_A - x)/x$ $(f_B - y)/y$	$f_A^{(s)}$ $f_B^{(s)}$	$f_A^{(d)}$ $f_B^{(d)}$	Tracer	$(f_A - x)/x$ $(f_B - y)/y$	$f_A^{(s)}$ $f_B^{(s)}$	$f_A^{(d)}$ $f_B^{(d)}$	Tracer	$(f_A - x)/x$ $(f_B - y)/y$
10	0.000	0.047	0.001	45.75	0.000	0.006	-0.012	-1.50	0.000	0.002	-0.015	-1.11
	0.088	0.037	0.097	0.29	0.184	0.003	0.188	-0.01	0.281	0.001	0.287	-0.02
20	0.000	0.127	0.097	0.31	0.000	0.110	0.027	3.06	0.000	0.057	0.009	5.33
	0.096	0.101	0.176	0.12	0.185	0.065	0.214	0.17	0.270	0.023	0.292	0.00
50	0.000	0.241	0.269	-0.10	0.000	0.150	0.187	-0.20	0.000	0.137	0.107	0.28
	0.133	0.193	0.315	0.04	0.192	0.090	0.307	-0.08	0.254	0.054	0.335	-0.08

were required to compute the mixing coefficients from SVD results, they were found to be in fair agreement with the mixing coefficients based on the dye concentration. The SVD based mixing estimation provides some insights into how the time-averaged and the unsteady components of the flow affect the overall mixing, as one can distinguish the contribution of individual modes. *E.g.* in Fig. 17 we see that the first two modes dominate by energy, and based on the flow fields in Fig. 15 and 16 one could evaluate mixing due to a given mode. Based on these results, PIV with SVD alone could be used to estimate mixing when the tracer technique (or planar laser induced fluorescence techniques) are unfeasible due to technical or cost constraints. A better estimate of mixing could be obtained from three-dimensional PIV measurements within the gap, or more planar PIV FOVs span the gap.

Notice

References

1. L. Meyer and K. Rehme. Large-Scale Turbulence Phenomena in Compound Rectangular Channels. *Exp. Therm. Fluid Sci.*, 8(4):286–304, 1994.
2. A. Mahmood, M. Rohde, T. H. J. J. van der Hagen, R. F. Mudde, T. van der Hagen, and R. F. Mudde. Contribution of Large-Scale Coherent Structures towards the Cross Flow in Two Interconnected Channels. In *NURETH-13*, Kanazawa, Japan, 2009.
3. F. Baratto, S. C. C. Bailey, and S. Tavoularis Measurements of frequencies and spatial correlations of coherent structures in rod bundle flows. *Nucl. Eng. Des.*, 236(17):1830-1837, 2006.
4. W. Eifler and R. Nijsing. Experimental investigation of velocity distribution and flow resistance in a triangular array of parallel rods. *Nucl. Eng. Des.*, 5:22–42, 1967.
5. T. Krauss. Characteristics of turbulent velocity and temperature in a wall channel of a heated rod bundle. *Exp. Therm. Fluid Sci.*, 12(1):75–86, jan 1996.
6. T. Krauss and L. Meyer. Experimental investigation of turbulent transport of momentum and energy in a heated rod bundle. *Nucl. Eng. Des.*, 180:185 – 206, 1998.
7. S. V. Moller. Single-Phase Turbulent Mixing in Rod Bundles. *Exp. Therm. Fluid Sci.*, pages 26–33, 1992.

8. L. Meyer. From discovery to recognition of periodic large scale vortices in rod bundles as source of natural mixing between subchannels-A review. *Nucl. Eng. Des.*, 240(6):1575–1588, 2010.
9. D. Chang and S. Tavoularis. Convective Heat Transfer in Turbulent Flow Near a Gap. *J. Heat Transfer*, 128(7):701, 2006.
10. D. Chang and S. Tavoularis. Numerical simulation of turbulent flow in a 37-rod bundle. *Nucl. Eng. Des.*, 237(6):575–590, mar 2007.
11. D. Home, G. Arvanitis, M. Lightstone, and M. Hamed. Simulation of flow pulsations in a twin rectangular subchannel geometry using unsteady Reynolds Averaged NavierStokes modelling. *Nucl. Eng. Des.*, 239(12):2964–2980, dec 2009.
12. J. Derksen. Simulations of lateral mixing in cross-channel flow. *Comput. Fluids*, 39(6):1058–1069, jun 2010.
13. D. Home and M. F. Lightstone. Numerical investigation of quasi-periodic flow and vortex structure in a twin rectangular subchannel geometry using detached eddy simulation. *Nucl. Eng. Des.*, 270:1–20, 2014.
14. E. Merzari, H. Ninokata, A. Mahmood, and M. Rohde. Proper orthogonal decomposition of the flow in geometries containing a narrow gap. *Theor. Comput. Fluid Dyn.*, 23(5):333–351, sep 2009.
15. J. Ko, D. Lucor, and P. Sagaut. Sensitivity of two-dimensional spatially developing mixing layers with respect to uncertain inflow conditions. *Phys. Fluids*, 20(7):077102, 2008.
16. S. A. Mäkiharju, S. L. Ceccio, J. R. Buchanan, A. G. Mychkovsky, K. J. Hogan, and K. T. Lowe. Experimental Characterization of Interchannel Mixing Through a Narrow Gap. In *Int. Top. Meet. Nucl. React. Therm. Hydraul.*, pages 4394–4409, 2015.
17. S. Yoon. *Electron Beam X-Ray Computed Tomography for Multiphase Flows and An Experimental Study of Interchannel Mixing*. PhD thesis, University of Michigan, 2017.
18. H. Schlichting. *Boundary-layer theory*. McGraw-Hill, 1968.
19. BIPM, IEC and IFCC, ILAC and IUPAC, IUPAP and ISO, OIML Evaluation of measurement dataguide for the expression of uncertainty in measurement.. *JCGM 100: 2008*, 2008.
20. G. Berkooz, P. Holmes, and J. L. Lumley The proper orthogonal decomposition in the analysis of turbulent flows. *Ann. Rev. Fluid Mech.*, 25(1):539–575, 1993.
21. M. P. Schultz, and K. A. Flack Reynolds-number scaling of turbulent channel flow. *Phys. Fluids*, 25(2):025104, 2013.